

1 New Methodology Shows Short Atmospheric Lifetimes of 2 Oxidized Sulfur and Nitrogen due to Dry Deposition

3 Katherine Hayden¹, Shao-Meng Li^{1,2*}, Paul Makar¹, John Liggio¹, Samar G. Moussa¹, Ayodeji
4 Akingunola¹, Robert McLaren³, Ralf M. Staebler¹, Andrea Darlington¹, Jason O'Brien¹, Junhua
5 Zhang¹, Mengistu Wolde⁴, Leiming Zhang¹

6 ¹*Air Quality Research Division, Environment and Climate Change Canada, Toronto, Ontario,*
7 *Canada, M3H 5T4*

8 ²*College of Environmental Science and Engineering, Peking University, Beijing 100871 China*

9 ³*Center for Atmospheric Chemistry, York University, 4700 Keele Street, Toronto, Ontario,*
10 *Canada*

11 ⁴*National Research Council Canada, Flight Research Laboratory, Ottawa, Canada K1A 0R6*

12 *corresponding authors shaomeng.li@pku.edu.cn; Katherine.hayden@canada.ca

13 For submission to *Atmospheric Chemistry and Physics*

14 Abstract

15
16 The atmospheric lifetimes of pollutants determine their impacts on human health, ecosystems
17 and climate and yet, pollutant lifetimes due to dry deposition over large regions have not been
18 determined from measurements. Here, a new methodology based on aircraft observations is used
19 to determine the lifetimes of oxidized sulfur and nitrogen due to dry deposition over $(3-6) \times 10^5$
20 km^2 of boreal forest in Canada. Dry deposition fluxes decreased exponentially with distance
21 from the Athabasca oil sands sources, located in northern Alberta, resulting in lifetimes of 2.2-26
22 hours. Fluxes were 2-14 and 1-18 times higher than model estimates for oxidized sulfur and
23 nitrogen, respectively, indicating dry deposition velocities which were 1.2-5.4 times higher than
24 those computed for models. A Monte-Carlo analysis with five commonly used inferential dry
25 deposition algorithms indicates that such model underestimates of dry deposition velocity are
26 typical. These findings indicate that deposition to vegetation surfaces are likely under-estimated
27 in regional and global chemical transport models regardless of the model algorithm used. The
28 model-observation gaps may be reduced if surface pH, and quasi-laminar and aerodynamic
29 resistances in algorithms are optimized as shown in the Monte-Carlo analysis. Assessing the air
30 quality and climate impacts of atmospheric pollutants on regional and global scales requires
31 improved measurement-based understanding of atmospheric lifetimes of these pollutants.

32

33 **1 Introduction**

34 Deposition represents the terminating process for most air pollutants and the starting
35 point for ecosystem impacts. Understanding deposition is critical in determining the atmospheric
36 lifetimes and spatial scale of atmospheric transport of pollutants, which in turn, dictates their
37 ecosystem (WHO, 2016; Solomon et al., 2007) and climate (Samset et al., 2014) impacts. In
38 particular, atmospheric lifetimes (τ) of oxidized sulfur and nitrogen compounds influence their
39 concentrations and column burdens in air, which affect air quality and hence human exposure
40 (WHO, 2016). Furthermore, the lifetime of these species affects their contributions to
41 atmospheric aerosols, with a consequent influence on climate via changes to radiative transfer
42 through scattering and cloud formation (Solomon et al., 2007). In addition, their deposition can
43 exceed critical load thresholds causing aquatic and terrestrial acidification, and eutrophication in
44 the case of nitrogen deposition (Howarth, 2008; Bobbink et al., 2010; Doney, 2010; Vet et al.,
45 2014; Wright et al., 2018). Quantifying τ and deposition thus provides a crucial assessment of
46 these regional and global impacts.

47 Deposition occurs through wet and dry processes. While wet deposition fluxes can be
48 measured directly (Vet et al., 2014), there are few validated methods for dry deposition fluxes
49 (Wesley and Hicks, 2000), and none which estimates deposition over large regions. Dry
50 deposition fluxes (F) may be obtained using micrometeorological measurements for pollutants
51 for which fast response instruments are available. However, these results are only valid for the
52 footprints of the observation sites, typically hundreds of meters (Aubinet et al., 2012), and their
53 extrapolation to larger regions may suffer from representativeness issues. As a result,
54 atmospheric lifetimes τ with respect to dry deposition have not been determined through direct
55 observations. On a regional scale, dry deposition fluxes are typically derived using an inferential

56 approach by multiplying network-measured or model-predicted air concentrations with dry
57 deposition velocities (V_d) (Sickles and Shadwick, 2015; Fowler et al., 2009; Meyers et al., 1991),
58 which are derived using resistance-based inferential dry deposition algorithms (Wu et al., 2018),
59 and compared with limited micrometeorological flux measurements (Wesley and Hicks, 2000;
60 Wu et al., 2018; Finkelstein et al., 2000; Matsuda et al., 2006; Makar et al., 2018) for validation.
61 When applied to a regional scale, an inferential-algorithm derived V_d may have significant
62 uncertainties (Wesley and Hicks, 2000; Aubinet et al., 2012; Wu et al., 2018; Finkelstein et al.,
63 2000; Matsuda et al., 2006; Makar et al., 2018; Brook et al., 1997). For example, inferred V_d for
64 SO₂, despite being the most studied and best estimated, may be underestimated by 35% for forest
65 canopies (Finkelstein et al., 2000). Underestimated V_d for SO₂ and nitrogen oxides can
66 contribute to model over-prediction of regional and global SO₂ concentrations (Solomon et al.,
67 2007; Christian et al., 2015; Chin et al., 2000), or under-prediction of global oxidized nitrogen
68 dry deposition fluxes (Paulot et al., 2018; Dentener et al., 2006).

69 Here, a new approach is presented to determine τ with respect to dry deposition and F for
70 total oxidized sulfur (**TOS**, the sulfur mass in SO₂ and particle-SO₄ (pSO₄)) and total reactive
71 oxidized nitrogen (**TON**, the nitrogen mass in NO, NO₂, and others designated as NO_x) on a
72 spatial scale of (3-6)x10³ km², using aircraft measurements. This approach provides a unique
73 methodology to determine τ and F over a large region. Coupled with analyses for chemical
74 reaction rates (for **TOS** compounds), the average V_d for **TOS** and **TON** over the same spatial
75 scale were also determined. The airborne measurements were obtained during an intensive
76 campaign from August to September 2013 in the Athabasca Oil Sands Region (AOSR) (Gordon
77 et al., 2015; Liggio et al., 2016; Li et al., 2017; Baray et al., 2018; Liggio et al., 2019) in northern

78 Alberta, Canada. Direct comparisons with modelled dry deposition estimates are made to assess
79 their uncertainties and the spatial-temporal scales of air pollutant impacts.

80 **2 Methods**

81 **2.1 Lagrangian Flight Design**

82 Details of the airborne measurement program have been described elsewhere (Gordon et
83 al., 2015; Liggio et al., 2016; Li et al., 2017; Liggio et al., 2019; Baray et al., 2018). Briefly, an
84 instrumented National Research Council of Canada's Convair-580 research aircraft was flown
85 over the AOSR in Alberta, Canada from August 13 to September 7, 2013. The flights were
86 designed to determine emissions from mining activities in the AOSR, assess their atmospheric
87 transformation processes and gather data for satellite and numerical model validation. Three
88 flights were flown to study transformation and deposition processes by flying a Lagrangian
89 pattern so that the same pollutant air mass was sampled at different time intervals downwind of
90 emission sources for a total of 4-5 hours and up to 107-135 km downwind of the AOSR sources.
91 Flights 7 (F7, Aug 19), 19 (F19, Sep 4) and 20 (F20, Sep 5) took place during the afternoon
92 when the boundary layer was well established. The flights were conducted in clear sky
93 conditions so wet deposition processes were insignificant. As shown in Figure 1, the aircraft
94 flew tracks perpendicular to the oil sands plume at multiple altitudes between 150 to 1400 m agl
95 and multiple intercepts of the same plume downwind. Vertical profiles conducted as spirals
96 were flown at the centre of the plume which provided information on the boundary layer height
97 and extent of plume mixing. The flight tracks closest to the AOSR intercepted the main
98 emissions from the oil sands operations; there were no other anthropogenic sources as the aircraft
99 flew further downwind of the AOSR.

100 2.2 Aircraft Measurements

101 A comprehensive suite of detailed gas- and particle-phase measurements were made from
102 the aircraft. Measurements pertaining to the analysis in this paper are discussed below.

103 **SO₂ and NO_y.** Ambient air was drawn in through a 6.35 mm (1/4") diameter PFA sampling line
104 taken from a rear-facing inlet located on the roof towards the rear of the aircraft. The inlet was
105 pressure-controlled to 770 mm Hg using a combination of a MKS pressure controller and a
106 Teflon pump. Ambient air from the pressure-controlled inlet was fed to instrumentation for
107 measuring SO₂ and NO_y. The total sample flow rate was measured at 4988 cm³ min⁻¹ of which
108 SO₂ and NO_y were 429 and 1085 cm³ min⁻¹, respectively. SO₂ was detected via pulsed
109 fluorescence with a Thermo 43iTLE (Thermo Fisher Scientific, Franklin, MA, USA). NO_y (also
110 denoted as Total Oxidized Nitrogen (TON)) was measured by passing ambient air across a
111 heated (325°C) molybdenum converter that reduces reactive nitrogen oxide species to NO. NO
112 was then detected through chemiluminescence with a modified Thermo 42iTTL (Thermo Fisher
113 Scientific, Franklin, MA, USA) run in NO_y mode. An inlet filter was used for SO₂ to exclude
114 particles, but NO_y was not filtered prior to the molybdenum converter. NO_y includes NO, NO₂,
115 HNO₃ and other oxides of nitrogen such as peroxy acetyl nitrate and organic nitrates (Dunlea et
116 al., 2007; Williams et al., 1998). Although there was no filter on the NO_y inlet to exclude
117 particles, the inlet was not designed to sample particles (i.e. rear-facing PFA tubing). As a result,
118 pNO₃ was not included as part of NO_y (TON) The conversion efficiency of the heated
119 molybdenum converter and inlet transmission was evaluated with NO₂ and HNO₃ and found to
120 be near 100% and >90%, respectively. Previous studies conducted by Williams et al. (1998)
121 showed similar molybdenum converter efficiencies including that of n-propyl nitrate near 100%.
122 Interferences from alkenes or NH₃ were assumed to be negligible (Williams et al., 1998; Dunlea

123 et al. 2007). Species like NO₃ radical and N₂O₅ are expected to be low in concentration as they
124 photolyze quickly during daytime. Zeros were performed 3-5 times per flight for both the SO₂
125 and NO_y instruments by passing ambient air through an in-line Koby King Jr cartridge for ~5
126 minutes. For the NO_y measurements pre-reactor zeroes (dynamic instrument zero) were also
127 obtained periodically throughout each flight using either ambient air or a Koby King Jr. air
128 purifier. Multiple calibrations were conducted before, during and after the study using National
129 Institute Standards and Technology reference standards. Data were recorded at a time resolution
130 of 1 second and corrected for a sampling time delay of 1-3 seconds depending on the instrument.
131 Detection limits were determined as 2 times the standard deviation of the values acquired during
132 zeroes; NO_y was 0.09 ppbv and SO₂ was 0.70 ppbv (Table S1).

133 **Aerosols.** Multiple aerosol instruments sub-sampled from a forward facing, shrouded, isokinetic
134 particle inlet (Droplet Measurement Technologies, Boulder, CO, USA). A Time-of-Flight High
135 Resolution Aerosol Mass Spectrometer (AMS) (Aerodyne Research Inc.) was used to measure
136 non-refractory submicron aerosol components including pSO₄, pNO₃, pNH₄, and p-organics.
137 Details of the AMS and its operations have been published elsewhere (DeCarlo et al., 2006).
138 The instrument was operated in mass spectrometry V-mode with a sampling time resolution of
139 10 seconds. Filtered measurements were taken 4-5 times per flight to determine background
140 signals. Detection limits of 0.048, 0.036, 0.235 and 0.236 $\mu\text{g m}^{-3}$ for pSO₄, pNO₃, pNH₄ and p-
141 organics were determined using 3 times the standard deviation of the average of filtered time
142 periods for all flights (Table S1). Ionization efficiency calibrations using monodisperse
143 ammonium nitrate were performed during the study with an uncertainty of $\pm 9\%$. Data were
144 corrected for a sampling time delay of 10 seconds by comparing with faster response instruments
145 e.g. a wing-mounted Forward Scattering Spectrometer Probe Model 300 (FSSP-300) and an in-

146 board Ultra High Sensitivity Absorption Spectrometer (UHSAS) (both from Droplet
147 Measurement Technologies). The FSSP and UHSAS instruments measure particle diameters
148 that range from 300 nm – 20 μm and 50 nm - 1 μm , respectively. The AMS data were processed
149 using AMS data analysis software (Squirrel, version 1.51H and PIKA, version 1.10H). The
150 particle collection efficiency (CE) of the AMS was determined through comparisons of the total
151 AMS-derived mass with the mass estimated from the size distribution measurements of the
152 UHSAS assuming a density based on the chemical composition. The CE for F7 and F20 was 0.5
153 for both flights, and for F19 it was 1.0. The CE was applied to all AMS species for the duration
154 of each flight (Figure S1). Since the AMS measures only particle mass < 1 μm (PM_{1}) in
155 diameter, the mass of SO_4 formed through OH oxidation was scaled upward to account for all
156 particle sizes that H_2SO_4 vapor could potentially condense on. The scaling factor was
157 determined using the surface area ratio of $\text{PM}_{1}/\text{PM}_{20}$ from the aircraft particle measurements,
158 assuming that the condensation process is approximately proportional to the surface area. PM_{1}
159 measurements were from the UHSAS and PM_{20} were from the FSSP300. As the ratio did not
160 vary significantly in the plumes, one single value was used between each set of screens; in F19
161 the ratio between screens ranged from 0.6 to 0.8, in F20 the ratio ranged from 0.8 to 0.9, and in
162 F7 the ratio ranged from 0.7 to 0.9 (Liggio et al., 2016).

163 Measurements are discussed in terms of total oxidized sulfur (TOS, the sulfur mass in SO_2 from
164 the Thermo SO_2 instrument and particle- SO_4 (pSO_4) from the AMS instrument) and total
165 reactive oxidized nitrogen (TON, the nitrogen mass in reactive oxidized nitrogen species, from
166 the Thermo NO_y instrument, often denoted NO_y).

167 **Volatile Organic Compounds (VOCs).** Selected VOCs were used to estimate the OH
168 concentrations used for determining oxidation rates for SO_2 . VOCs were measured with a proton

169 transfer reaction time-of-flight mass spectrometer (PTR-ToF-MS, Ionicon Analytik GmbH,
170 Austria) as well as through discrete canister grab samples. The PTR-ToF-MS and its operation,
171 along with the details of the canister sampling and lab analyses during the study were described
172 in detail previously (Li et al., 2017). Briefly, the PTR-ToF-MS used chemical ionization with
173 H_3O^+ as the primary reagent ion. Gases with a proton affinity greater than that of water were
174 protonated in the drift tube. The pressure and temperature of the drift tube region were
175 maintained at a constant 2.15 mbar and 60°C, respectively for an E/N of 141 Td (Townsend, 1
176 $\text{Td}=10^{-17} \text{ V cm}^2$). E/N refers to the reduced electric field parameter in the drift tube; E is the
177 electric field and N is the number density of the gas in the drift tube. The E/N ratio can affect the
178 reagent ion distribution in the drift tube and VOC fragmentation (de Gouw and Warneke; 2007).
179 The protonated gases were detected using a high-resolution time of flight mass spectrometer at a
180 time resolution of 2 seconds. Instrumental backgrounds were performed in flight using a
181 custom-built zero-air generating unit. The unit contained a catalytic converter heated to 350°C
182 with a continuous flow of ambient air at a flow rate of one litre per minute. The data were
183 processed using Tofware software (Tofwerk AG). Calibrations were performed on the ground
184 using gas standard mixtures from Ionicon, Apel-Reimer and Scott-Marrin for 22 compounds.
185 The canister samples were collected in pre-cleaned and passivated 3L stainless steel canisters
186 that were subsequently sent to an analytical laboratory for GC-FID/MS analyses for a suite of
187 150 hydrocarbon compounds.

188 **Meteorology and aircraft state parameters.** Meteorological measurements have been
189 described elsewhere (Gordon et al., 2015). In brief, 3-D wind speed and temperature were
190 measured with a Rosemount 858 probe. Dew point was measured with an Edgetech hygrometer
191 and pressure was measured with a DigiQuartz sensor. Aircraft state parameters including

192 positions and altitudes were measured with GPS and a Honeywell HG1700 unit. All
193 meteorological measurements and aircraft state parameters were measured at a 1 s time
194 resolution.

195

196 **2.3 Mass transfer rates in the atmosphere**

197 Mass transfer rates (T) across flight screens (Figure 1) were determined using an
198 extension of the Top-down Emission Rate Retrieval Algorithm (TERRA) developed for emission
199 rate determination using aircraft measurements (Gordon et al., 2015). Briefly, at each plume
200 interception location, the level flight tracks were stacked to create a virtual screen. Background
201 subtracted pollutant concentrations and horizontal wind speeds normal to the screen were
202 interpolated using kriging. The background for SO_2 was ~ 0 ppb and pSO_4 was $0.2 - 0.3 \mu\text{g m}^{-3}$
203 which was subtracted from the pSO_4 measurements before mass transfer rates were calculated
204 (Liggio et al., 2016). Integration of the horizontal fluxes across the plume extent on the screen
205 yields the transfer rate T in units of t hr^{-1} . Using SO_2 as an example,

$$206 \quad T_{\text{SO}_2} = \int_{s_1}^{s_2} \int_{z_1}^{z_2} C(s, z) u_n(s, z) ds dz \quad (1)$$

207 where $C(s, z)$ is the background subtracted concentration at screen coordinate s and z , which
208 represent the horizontal and vertical axes of the screen. The $u_n(s, z)$ is the horizontal wind speed
209 normal to the screen at the same coordinates.

210 Since the lowest flight altitude was 150 magl, it was necessary to extrapolate the data to
211 the surface as per the procedures described previously (Gordon et al., 2015). Extrapolation to the
212 surface methods were compared and differences were included in the uncertainty estimates. The
213 main sources of SO_2 were from elevated facility stacks associated with the desulfurization of the

214 raw bitumen (Zhang et al., 2018). The stacks with the biggest SO₂ emissions range in height
 215 from 76.2 to 183.0 m. Since the main source of SO₂ is from the elevated facility stacks, the
 216 uncertainty for a single screen is estimated at 4% (Gordon et al., 2015). NO_y was also
 217 extrapolated linearly to the surface and the mass transfer rates were similarly compared to other
 218 extrapolation methods. NO_y sources include the elevated facility stacks and surface sources such
 219 as the heavy hauler trucks operating in the surface mines. The uncertainty in the resulting
 220 transfer rate T for a single screen is estimated to be larger at 8%, as a larger fraction of the NO_y
 221 mass may be below the lowest measurement altitude (Gordon et al., 2015). Sulfur and nitrogen
 222 data were also extrapolated linearly to background values from the highest altitude flight tracks
 223 upwards to the mixed layer height, which was determined from vertical profiles of pollutant
 224 mixing ratios, temperature and dew point (Table 1).

225 Changes in the mass transfer rate T (denoted ΔT) in units of t hr⁻¹ were then calculated as
 226 the differences in T between pairs of virtual screens. The uncertainty in ΔT was estimated as 8%
 227 for **TOS** and 26% for **TON** as supported by emission rate uncertainties determined for box
 228 flights (Gordon et al., 2015). The uncertainty analysis for box flights is applicable to ΔT here, as
 229 both account for uncertainties with an upwind and a downwind screen. The ΔT uncertainties
 230 were propagated through subsequent calculations.

231 Knowing the change in mass transfer rate ΔT , and accounting for the net rates of
 232 chemical loss and formation between screens for SO₂ and pSO₄, the deposition rates (and
 233 subsequently the deposition flux in tonnes S (or N) km⁻² hr⁻¹, Section 2.4 were determined for the
 234 sulfur compounds as follows:

$$235 \quad \Delta T_{SO_2} = T_{SO_2}(t_2) - T_{SO_2}(t_1) = X_{SO_2} - D_{SO_2} \quad (2)$$

$$236 \quad \Delta T_{pSO_4} = T_{pSO_4}(t_2) - T_{pSO_4}(t_1) = X_{pSO_4} - D_{pSO_4} \quad (3)$$

237
$$\Delta T_{TOS} = T_{TOS}(t_2) - T_{TOS}(t_1) = -D_{TOS} \quad (4)$$

238 where X_{SO_2} is the rate of chemical reaction loss of sulfur mass in SO_2 , X_{pSO_4} is the rate of
239 chemical formation of sulfur mass as pSO_4 , D_{SO_2} and D_{pSO_4} are deposition rates of sulfur mass in
240 SO_2 and pSO_4 respectively, and t_1 and t_2 are plume interceptions times at Screen 1 and Screen 2,
241 respectively. Note that the chemical loss rate of SO_2 is set to be equivalent to the formation rate
242 of pSO_4 i.e. $X_{SO_2} = X_{pSO_4}$. Equation 4 for TOS can also similarly be written as shown in Equation
243 5.

244
$$\Delta T_{TOS} = \Delta T_{SO_2} + \Delta T_{pSO_4} = -D_{SO_2} - D_{pSO_4} \quad (5)$$

245 Units in Equations 2 to 5 are all in $t\ hr^{-1}$. Reaction with the OH radical was considered to be the
246 most significant chemical loss of SO_2 and the most significant path for the formation of pSO_4 .
247 X_{SO_2} and X_{pSO_4} were determined using estimated OH radical concentrations, which were
248 estimated using the methodology described in SI Section S4. Although TON encompasses a
249 range of different N species with expected differences in their deposition rates, it was not
250 possible to quantitatively separate their chemical formation/losses from their deposition rates
251 with this method. For total oxidized sulfur **TOS** (i.e., sulfur in $SO_2 + pSO_4$) and total oxidized
252 nitrogen **TON** (i.e., nitrogen in NO_y) the chemistry term is not relevant, and thus, the dry
253 deposition rate D_{TOS} was directly determined from ΔT_{TOS} using equation (4), and respectively for
254 **TON**.

255

256 **2.4 Dry deposition fluxes and dry deposition velocities**

257 Average dry deposition fluxes (F) for **TOS** and **TON** were obtained by dividing the
258 deposition rates D in $t\ hr^{-1}$ with the footprint surface area of the plume between two adjacent

259 screens (Figure 1 grey shaded regions), as shown in Equation 6 for the dry deposition flux F_{TOS}
260 of **TOS** (in t S km⁻² hr⁻¹):

$$261 \quad F_{TOS} = \frac{D_{TOS}}{Area} \quad (6)$$

262 where the surface area, *Area*, was identified as the geographic area under the plume extending to
263 the edges of the plume where concentrations fell to background levels (i.e. SO₂ to ~0 ppb; SO₄
264 ~0.2 ug m⁻³). This approach was similarly used to derive deposition fluxes from an air quality
265 model, Global Environmental Multiscale – Modelling Air-quality and Chemistry (GEM-MaCH)
266 (Moran et al., 2010; also see SI Section S5 for details). The geographic surface area uncertainty
267 is estimated at 5%. Dry deposition fluxes between the sources and the first screen were also
268 estimated using change in mass transfer rate ΔT based on the extrapolated transfer rates back to
269 the source region ('extended' region). The surface area boundaries for these 'extended' regions
270 were determined using latitude and longitude coordinates that were weighted by emissions. This
271 was done by first using the average wind direction from Screen 1 and creating a set of parallel
272 back trajectories (~20) starting at different parts of Screen 1 back across the source region. For
273 **TON**, the NO_x emission sources along each back trajectory were weighted by their NO_x
274 emissions to obtain an emissions-weighted center location with latitude and longitude
275 coordinates for each back trajectory. The line connecting these emissions-weighted center
276 locations formed the boundary of the extended surface area. The extended surface area was
277 similarly determined for **TOS** based upon the known locations of the major SO₂ point sources.
278 The uncertainty of the 'extended' regions is estimated at 10% based on repeated optimizations of
279 the geographical area. Surface areas are visualized as grey shaded regions between screens in
280 Figure 1 and tabulated in SI Table S1.

281 Spatially-averaged dry deposition velocities, V_d , based on the aircraft measurements were
282 determined over the surface area between screens using average plume concentrations across
283 pairs of screens at about 40 meters above the ground for **SO₂** and **TON** (e.g. Equation 7 for SO₂
284 in units of cm s⁻¹). Although TOS includes the S in both SO₂ and pSO₄, only SO₂ is used in the
285 calculation of V_d since the deposition behaviour of gases and particles differ substantially, and
286 particles additionally have size-dependent deposition rates (Emerson et al., 2020). As the
287 dominant form of TOS is SO₂ (>92%) the deposition behaviour of TOS is expected to be largely
288 driven by that of SO₂. The measured TON does not include pNO₃.

$$289 \quad V_d = \frac{F_{SO_2}}{[SO_2]} \quad (7)$$

290 The largest source of uncertainty in V_d calculated this way was the determination of
291 concentration at 40 meters above the surface as the measurements were extrapolated from the
292 lowest aircraft altitude to the surface and interpolated concentrations were used. The
293 measurement-derived V_d are compared with those from the air quality model GEM-MACH
294 which uses inferential methods.

295

296 **2.5 Monte-Carlo simulations of dry deposition velocities using multiple resistance-based** 297 **parameterizations**

298 Parameterization of dry deposition in inferential algorithms is commonly based on a
299 resistance approach with dry deposition velocity depending on three main resistance terms as
300 below:

301
$$V_d = \frac{1}{R_a + R_b + R_c} \quad (8)$$

302

303 where R_a , R_b and R_c represent the aerodynamic, quasi-laminar sublayer and bulk surface
304 resistances respectively. Although these resistance terms are common among many regional air
305 quality models (Wu et al., 2018), the formulae used (and inputs in to these formulae) to calculate
306 the individual resistance terms differ significantly among the inferential deposition algorithms.
307 To assess the potential for a general underestimation of V_d across different inferential deposition
308 algorithms, and to compare with the aircraft-derived V_d , five different inferential deposition
309 algorithms, including that used in the GEM-MACH model for calculating V_d (Wu et al., 2018)
310 were incorporated into a Monte-Carlo simulation for V_d for SO_2 . NO_y was not considered here,
311 as its measurement includes multiple reactive nitrogen oxide species with different individual
312 deposition velocities. We note that many of the inferential algorithms are based on observations
313 of SO_2 and O_3 deposition made at single sites, and the extent to which a chemical is similar to
314 SO_2 or O_3 features into its V_d calculation – the comparison thus has relevance for species aside
315 from SO_2 . The five deposition algorithms considered are denoted ZHANG, NOAH-GEM,
316 C5DRY, WESLEY and GEM-MACH and are compared in Wu et al. (2018) (except the
317 algorithm in GEM-MACH). The five algorithms all use a big-leaf approach for calculating V_d
318 i.e. V_d is based on the resistance-analogy approach for calculating dry deposition velocity where
319 V_d is the reciprocal sum of three resistance terms R_a , R_b and R_c . Although the approach is
320 similar, the formulations of R_a , R_b and R_c between the algorithms are substantially different
321 (Table 1 in Wu et al., 2018). Results from Wu et al (2018) suggest that the differences in R_a+R_b
322 between different models would cause a difference in their V_d values on the order of 10-30% for

323 most chemical species (including SO₂ and NO₂), although the differences can be much larger for
324 species with near-zero R_c such as HNO₃.

325 To perform the simulations, formulae for the first four algorithms were taken from Wu et
326 al. (2018) and for GEM-MACH taken from Makar et al. (2018). The stomatal resistance in the
327 ZHANG algorithm was from Zhang et al. (2002). The GEM-MACH formula (Equation 8.7 in
328 the SI of Makar et al. (2018)) for mesophyll resistance R_{mx} contained a typo (missing the Leaf
329 Area Index (LAI)) and was corrected for as follows:

$$330 R_{mx} = [LAI(H^*/3000 + 100 f_0)]^{-1} \quad (9)$$

331 Prescribed input values were constrained by the range of possible values consistent with the
332 conditions during the aircraft flights and are shown in SI Table S3 with associated references.
333 Calculations for the R_a term were based on unstable and dry conditions as observed during the
334 aircraft flights. The Monte-Carlo simulation generated a distribution of possible V_a values,
335 based on randomly generated values of the input variables to each algorithm and selected from
336 Gaussian distributions with a range of 3 sigma for all input parameters. All simulations were
337 performed with the same input values that were common between the algorithms.

338 **3 Results and Discussion**

339 **3.1 Meteorological and Emissions Conditions during the Transformation Flights**

340 Three aircraft flights, Flights 7 (F7), 19 (F19) and 20 (F20) were conducted in
341 Lagrangian patterns where the same plume emitted from oil sands activities was repeatedly
342 sampled for a 4-5 hour period and up to 107-135 km downwind of the AOSR. The first screen of
343 each flight captured the main emissions from the oil sands operations with no additional
344 anthropogenic sources between subsequent screens downwind. The main sources of nitrogen

345 oxides were from exhaust emissions from off-road vehicles used in open pit mining activities and
346 sulfur and nitrogen oxides from the elevated facility stack emissions associated with the
347 desulfurization of raw bitumen (Zhang et al., 2018). As depicted in Figure 1, F7 and F19
348 captured a plume that contained both sulfur and nitrogen oxides. The westerly wind direction
349 and orientation of the aircraft tracks on F20 resulted in the measurement of two distinct plumes;
350 one plume exhibited increased levels of sulfur and nitrogen oxides mainly from the facility
351 stacks, and the other plume contained elevated levels of nitrogen oxides, mainly from the open
352 pit mining activities, and no SO₂.

353 During the experiments, the dry deposition rates (D) (t hr⁻¹) were quantified under
354 different meteorological conditions and emissions levels of **TOS** and **TON** (E_{TOS} and E_{TON}) for
355 the three flights (see Table 1). These differences played important roles in the observed pollutant
356 concentrations and resulting dry deposition fluxes for F7, F19 and F20. Mixed layer heights
357 (MLH) were derived from aircraft vertical profiles that were conducted in the centre of the
358 plume at each downwind set of transects. The profiles of temperature, dew point temperature,
359 relative humidity and pollutant mixing ratios were inspected for vertical gradients indicating a
360 contiguous layer connected to the surface. The highest MLH was determined for F7 at 2500
361 magl whereas F19 had the lowest MLH at 1200 magl (Table 1). In F20, the MLH was 2100
362 magl. The combination of a high MLH in F7 with the highest wind speeds resulted in the lowest
363 pollutant concentrations of the three flights. In F19, lower wind speeds and the lowest mixed
364 layer heights led to the highest pollutant levels. F20 had emissions and meteorological
365 conditions that were in between F7 and F19 resulting in pollutant concentrations between those
366 of F7 and F19.

367 Emission rates of SO₂ and NO_x (designated as *E_{TOS}* and *E_{TON}*) from the main sources in
368 the AOSR were estimated from the aircraft measurements and varied significantly between the
369 three flight days. The measurement-based emission rates of *E_{TOS}* and *E_{TON}* were taken from the
370 mass transfer rates of *T_{SO2}* and *T_{NOy}* (described in Methods) by extrapolating backwards to the
371 source locations in the AOSR using exponential functions (Figure 2, Section 3.2). For **TOS**, the
372 source location was set at 57.017N, -111.466W, where the main stacks for SO₂ emissions are
373 located. For **TON**, the source locations were determined from geographically weighted
374 locations. Emission rates *E_{TOS}* and *E_{TON}* for each flight are shown in Table 1.

375 Model-based *E_{TOS}* and *E_{TON}* were also obtained from the 2.5 km x 2.5 km gridded
376 emissions fields that were specifically developed for model simulations of the large AOSR
377 surface mining facilities (Zhang et al., 2018) i.e. Suncor Millennium, Syncrude Mildred Lake,
378 Syncrude Aurora North, Shell Canada Muskeg River Mine & Muskeg River Mine Expansion,
379 CNRL Horizon Project and Imperial Kearn Mine. The emissions fields have been used in GEM-
380 MACH (described in SI Section S5) to carry out a number of model simulations (Zhang et al.,
381 2018; Makar et al., 2018) including for the present study. In this work, emissions were summed
382 from various sources including offroad, point (Continuous Emissions Monitoring (CEMS)), and
383 point (non-CEMS) for the surface mines to obtain total AOSR hourly emission rates for the
384 flight time periods of interest (Table 2). The standard deviations reflect the emissions variations
385 during the simulated flight.

386 **3.2 Mass Transfer Rates**

387 The mass transfer rates *T* (in t hr⁻¹) across the virtual flight screens for all three flights are
388 shown for **TOS** and **TON** in Figure 1 and plotted in Figure 2. In F20, two distinct **TON** plumes
389 were observed, allowing separate *T* calculations for **TON**. Monotonic decreases in *T* were

390 observed for both **TOS** and **TON** during transport downwind in all flights, clearly showing dry
391 depositional losses. The deposition rate D (Methods, Section 2.3) was used to estimate the
392 cumulative deposition of **TOS** and **TON** as a fraction of E_{TOS} or E_{TON} and is shown in Figure 3
393 for F7, F19 and F20 for transport distances of up to 107-135 km downwind of the sources.
394 Curves were fitted to the **TOS** and **TON** dry deposition cumulative percentages from which $d_{1/e}$
395 and τ were determined (SI Table S1). The transport e-folding distance ($d_{1/e}$) was determined
396 where 63.2% of E_{TOS} (or E_{TON}) was dry deposited, i.e., $\sum_{d=0}^{d_{1/e}} D(d) = 0.368E_{TOS}$. The
397 atmospheric lifetimes (τ) were derived as $\tau = d_{1/e}/u$, where u was the average wind speed across
398 the distance $d_{1/e}$. These estimates were compared with predictions from the regional air quality
399 model GEM-MACH (Makar et al., 2018; Moran et al., 2010; SI Section S5) using facility
400 emission rates (Table 2). For **TOS** during F19, (Figure 3b, e), the observed cumulative
401 deposition at the maximum distance accounted for 74±5% vs. the modelled 21% of E_{TOS} . The
402 measurements indicate that the cumulative deposition of **TOS** was due mostly to SO_2 dry
403 deposition where SO_2 was ~100% of **TOS** closest to the oil sands sources decreasing to 94%
404 farthest downwind. Although the modelled cumulative deposition of **TOS** was significantly
405 lower than the observations, the fractional deposition of SO_2 was similar, decreasing from
406 ~100% to 95% of **TOS**. Fitting a curve to D and interpolating the cumulative deposition fraction
407 to the 63.2% E_{TOS} loss leads to a $d_{1/e}$ of 71±1 km, versus 500 km for the model prediction.
408 Under the prevailing wind conditions, the observed distance indicates a τ for **TOS** of
409 approximately 2.2 hours, whereas the model prediction indicated 16 hours. Large observation-
410 based values and model prediction differences in lifetime were also evident for the other flights
411 (SI Table S1). Clearly, the model predictions significantly underestimated deposition and vastly
412 overestimated $d_{1/e}$ and τ . The observation-based values for τ are also lower than average

413 lifetimes of 1–2 days for SO₂ and 2–9 days for pSO₄ derived from global models (Chin et al.,
414 2000; Benkovitz et al., 2004; Berglen et al., 2004), which include the effects of wet deposition
415 and chemical conversion for SO₂, thus making their implicit residence times with respect to dry
416 deposition even longer.

417 For **TON** in F19 (Figure 3h, l), the observed cumulative deposition accounted for
418 $49 \pm 11\%$ of E_{TON} at the maximum flight distance, versus 19% predicted by the model. Similar
419 model underestimates for cumulative deposition fractions were found for F7 and F20.
420 Extrapolating to the 63.2% cumulative deposition fraction, $d_{1/e}$ was estimated to be 190 ± 7 km for
421 F19 versus a predicted 650 km from the model, implying a τ of approximately 5.6 hours for the
422 measurement-based results and 23 hours for the model prediction. Again, analogous differences
423 for F7 and F20 were found (SI Table S1). Similar to TOS, the measurement-based $d_{1/e}$ and τ
424 values for TON were significantly smaller than commonly accepted lifetimes of a few days for
425 nitrogen oxides in the boundary layer (Munger et al., 1998).

426 **3.3 Dry Deposition Fluxes F**

427 Using the deposition rate D (in tonnes S or N hr⁻¹), the average dry deposition fluxes, F
428 (in tonnes S or N km⁻² hr⁻¹), were calculated by dividing D by the plume footprint surface areas
429 estimated by extending to the plume edges where the concentrations fell to background levels
430 (Methods, Section 2.4). These footprints are shown as the gray shaded geographic areas in
431 Figure 1, totaling 3500, 5700 and 4200km² for F7, F19, and F20 plumes, respectively; see SI
432 Table S1 for **TON** plume areas). Figure 4a shows F_{TOS} values for all three flights, exhibiting
433 exponential decreases with increasing distance away from the sources and showing e-folding
434 distances for F_{TOS} of 18, 27, and 55 km for F7, F19, and F20, respectively. More than 90% of
435 the decreases in F_{TOS} were accounted for by F_{SO_2} . Similarly, F_{TON} decreased exponentially with

436 increasing transport distances in all flights (Figure 4c), exhibiting e-folding distances of 18 and
437 33 km for F7 and F19, and 55 and 189 km for the south and north **TON** plumes during F20,
438 respectively. These e-folding distances were similar to those for F_{TOS} , indicating similar rates of
439 decreases in F_{TON} with transport distances.

440 The potential for other processes to contribute to the derived TOS and TON fluxes were
441 considered including losses from the boundary layer to the free troposphere and re-emission of
442 TOS or TON species from the surface back to the gas-phase. Two different approaches, a finite
443 jump model and a gradient flux approach (Stull, 1988; Degrazia et al., 2015), were used to
444 estimate the potential upward loss across the interface between the boundary layer and the free
445 troposphere for sulfur and nitrogen. In both approaches, the upward S flux was a minor loss at <
446 $45 \text{ g km}^{-2} \text{ hr}^{-1}$, about 3 orders of magnitude lower than the several to many $\text{kg km}^{-2} \text{ hr}^{-1}$
447 horizontal advective transport that were determined using TERRA. For N, the upward flux
448 was estimated to be $\sim 570 \text{ g km}^{-2} \text{ hr}^{-1}$, so although a larger flux than S, it is about factor of 18
449 lower than the TON fluxes derived from observations.

450 As expected from the τ and transport e-folding distance $d_{1/e}$ comparisons, the GEM-
451 MACH model F_{TOS} were significantly lower than the measurement-based F_{TOS} results (Figure
452 4a), with the model F_{TOS} e-folding distances usually large: 133, 797, and 57 km for F7, F19, and
453 F20, respectively, or 7.4, 29.5, and 1.1 times longer than the corresponding measurement results.
454 Part of the differences between model and measurement F_{TOS} could be explained by differences
455 in actual versus model emissions, E_{TOS} (Tables 1 vs 2). To remove the influence of emissions,
456 an emission-normalized flux ($=F_{TOS}/E_{TOS}$ and F_{TON}/E_{TON}) was calculated for both measurement
457 and model (SI Figure S2). Figure 4b shows the ratios of measurement to model normalized
458 emissions for TOS. The model emission-normalized fluxes F_{TOS}/E_{TOS} were lower than the

459 measurement-based values by factors of 2.5-14, 1.8-3.4, and 2.0-3.0 for F7, F19, and F20,
460 respectively, decreasing with increased transport distances. However, they coalesce to a factor
461 of 2 at the furthest distances sampled by the aircraft, indicating that the model F_{TOS} estimates
462 were biased low by similar factors. The decreasing trends suggest that at distances further
463 downwind, model fluxes may exceed measurement-based fluxes, albeit at magnitudes lower than
464 those shown in Figure 4a, which is consistent with earlier study results (Makar et al., 2018). For
465 F_{TON} , the model-predicted values were also lower than the measurement results, especially near
466 the sources (Figure 4c), and showed little variation with transport distances from the oil sands
467 sources for all flights, in strong contrast to the exponential decays observed from the aircraft.
468 However, the emission-normalized fluxes ($=F_{TON}/E_{TON}$) for the model approached those from
469 measurements within maximum flying distances for F19 and F20, although still significantly
470 lower for F7 (>10x) (Figure 4d).

471 **3.4 Dry Deposition Velocities V_d**

472 The shorter $d_{1/e}$ and τ , and larger deposition fluxes F near the sources determined from
473 the aircraft measurements compared to predictions by the GEM-MACH model indicate that the
474 model dry deposition velocities V_d was underestimated. Gas-phase V_d in the model is predicted
475 with a standard inferential “resistance” algorithm (Wesley, 1989; Jarvis, 1976), with resistance to
476 deposition calculated for multiple parameters including aerodynamic, quasi-laminar sublayer and
477 bulk surface resistances (Baldocchi, 1987). To demonstrate the model underestimation in V_d ,
478 comparisons between the measurement-based and model V_d were made where an evaluation of
479 V_d for TOS and TON was possible. All F_{SO_2} were converted into V_{d,SO_2} by dividing F_{SO_2} by
480 interpolated SO_2 concentrations at 40 meters above ground, averaging 1.2 ± 0.5 , 2.4 ± 0.4 , and
481 3.4 ± 0.6 $cm\ s^{-1}$ for F7, F19 and F20, respectively, across the plume footprints (Methods, Section

482 2.4 and SI Table S2). The corresponding model V_{d-SO_2} derived in the same way as the
483 observations was 0.72, 0.63, and 0.58 cm s^{-1} , 1.7-5.4 times lower than observations (SI Section
484 S5; SI Table S2). Interestingly, the median V_d for SO_2 of 4.1 cm s^{-1} determined using eddy
485 covariance/vertical gradient measurements from a tower in the AOSR is higher than the mass
486 balanced method showing an even larger discrepancy compared to the model (SI Section S3;
487 Figure S5). Similarly, derived V_{d-TON} averaged 2.8 ± 0.8 , 1.6 ± 0.5 , 4.7 ± 1.4 and 2.2 ± 0.7 cm s^{-1} F7,
488 F19, F20 south plume, and F20 north plume, respectively (SI Table S2), 1.2-5.2 times higher
489 than the corresponding modelled V_{d-TON} of 1.4, 1.3, 0.92, and 0.90 cm s^{-1} .

490 Using the observations, it was not possible to derive individual TON deposition rates
491 separate from their chemical formation/losses. In previous modelling work, Makar et al. (2018),
492 use the GEM-MACH model and describe the relative contributions of different TOS and TON
493 species towards total S and N deposition in the AOSR. TON was dominated by dry NO_2 (g)
494 deposition fluxes close to the sources (>70% of total N close to the sources), and dry HNO_3 (g)
495 deposition increases with increasing distance from the sources (remaining < 30% of total N), and
496 other sources of TON having minor contributions to deposition (< 10%). Although TON
497 encompasses a range of different N species with expected differences in their deposition rates,
498 comparisons of V_{d-TON} with the model show, nevertheless, that overall large differences do exist.

499 **3.5 Monte-Carlo simulations of V_d for SO_2**

500 To further demonstrate observation-model differences, V_d distributions of SO_2 from five
501 common inferential dry deposition algorithms (Wu et al., 2018; Makar et al., 2018) were
502 determined for the conditions encountered during the flights using a Monte-Carlo approach as
503 described in Methods, Section 2.5). Results for the V_d simulations algorithms are shown in
504 Figure 5a. Histograms for all five algorithms have peak V_d values at ~ 1 cm s^{-1} or lower.

505 Probability distributions for the individual resistance terms, R_a , R_b , and R_c showed that the
506 dominant resistance driving V_d was the R_c term (SI Figure S3). Also shown in Figure 5a are the
507 measurement-derived V_d for Flights 7, 19 and 20, and that from the Oski-ötin ground site. The
508 observed V_d values are larger than the V_d values for most of the simulations, with the exception
509 of Flight 7, where the Zhang et al. (2002), NOAA-GEM (Wu et al., 2018) and C5DRY (Wu et
510 al., 2018) algorithms' distributions agree with the observations. All algorithms are biased low
511 relative to the observations for the remaining flights, and the Oski-ötin ground site. It is noted
512 that the ground-site observations that were derived using a standard flux tower methodology (SI
513 Section S3) at a single site, appeared to be higher than all other V_d ; nevertheless, these
514 observations are closer to the aircraft values than the algorithm estimates. These results indicate
515 that an underestimation of V_d relative to both aircraft and ground based measurements in the
516 AOSR is not unique to the GEM-MACH model or its dry deposition algorithm; similar results
517 would occur with the other algorithms included in the Monte-Carlo simulations, all of which are
518 used within other regional models.

519 To investigate the possible reasons behind the low model V_d relative to the observations,
520 a series of sensitivity tests using SO_2 were conducted. Differences in model V_d have been shown
521 to be mainly due to differences in the calculated R_c (Wu et al., 2018), and sensitivity tests here
522 indicated that R_c is particularly sensitive to the cuticular resistance R_{cut} . Hence, factors causing
523 R_{cut} to change can have significant impact on model V_d . In some of the algorithms, R_{cut} and
524 other resistance terms are dependent on the effective Henry's Law constant K_H^* for SO_2 . The
525 Monte-Carlo simulations for Figure 5 assumed a surface pH= 6.68 resulting in a K_H^* of 1×10^5 for
526 SO_2 . Additional Monte-Carlo simulations were performed for the GEM-MACH dry deposition
527 algorithm by adjusting K_H^* assuming different pH with small variations from a pH=6.68

528 significantly changing R_c , R_{cut} , and V_d (SI Figure S4). In Figure 5b – red dashed line, with a
529 surface pH change from 6.68 to 8, consistent with possible alkaline surfaces in the AOSR
530 (Makar et al., 2018), in the GEM-MACH simulation, the V_d distribution is moved to larger
531 values) with its peak value shifting from 0.6 to 1.4 cm s^{-1} . These results show that model V_d may
532 be highly sensitive to assumed surface pH, at least when using some inferential dry deposition
533 algorithms which are pH-dependent. However, Figure 5b shows that this pH-associated increase
534 in V_d is still insufficient to encompass the range of measurement-derived V_d . Increasing pH to 8
535 for the GEM-MACH simulation reduces R_{cut} , hence R_c , to values much smaller than R_a and R_b ,
536 suggesting that model V_d cannot further increase without reductions in both R_a and R_b . In other
537 words, R_a and R_b were probably overestimated in the current deposition velocity algorithms. By
538 using the Zhang et al. (2002) R_a and the NOAH-GEM (Wu et al., 2018) R_b parameterizations in
539 the GEM-MACH algorithm, a further shift of the GEM-MACH V_d distribution to larger values
540 was found, with the range encompassing most of the observations (Figure 5b, pink dashed line).

541 Using the Zhang and NOAH-GEM parameterizations, rather than the GEM-MACH
542 parameterization, would decrease the R_a and R_b for the momentum, heat and moisture fluxes as
543 well, but still remain within the range of what is expected based on published parameterizations
544 (Wu et al., 2018 and references therein).

545 The potential for re-emission of TOS and TON species was also considered. Fulgham et
546 al. (2020) report that the bidirectional fluxes of volatile organic acids are driven by an
547 equilibrium partitioning between surface wetness and the atmosphere. The observations
548 presented here represent the net flux of all processes including the effects of deposition and any
549 potential re-emissions of TOS and TON compounds should this process occur. As the results
550 show a net downward flux (i.e. net deposition), if any re-emission was occurring, it would be

Formatted: Subscript

Formatted: Subscript

551 smaller than the deposition fluxes observed here, which are themselves higher than shown by
552 currently available deposition algorithms. This implies that the deposition part of the flux must
553 be even larger than the net observed flux and the measured net fluxes presented here should then
554 be considered as minimum values. The current deposition algorithms do not include
555 bidirectional fluxes for inorganics, and adjustments related to pH in some situations may not be
556 sufficient to parameterize deposition fluxes. A bidirectional approach may be needed that would
557 include not only $[H^+]$, but surface heterogeneous reactions, to determine near-surface equilibrium
558 concentrations of co-depositing gases such as ammonia and nitric acid.

559 It is clear from the Monte-Carlo simulations for SO_2 V_d comparisons, inferential dry
560 deposition algorithms as used in regional and global chemical transport models need to be further
561 validated and improved, especially over large geographic regions. Here, the role of pH was
562 identified for improvement in some algorithms along with possible improvement in aerodynamic
563 and quasi-laminar sublayer resistance parameters. Yet, for other algorithms and for **TON**
564 compounds, the model low-biases in V_d remain to be investigated.

565 The underestimates suggest that the applications of these algorithms in regional or global
566 models may significantly underestimate predictions of **TOS** dry depositional loss from the
567 atmosphere. Underestimates in V_d are the result of a combination of uncertainties in the
568 parameterizations of each algorithm. In the case of the algorithm used in GEM-MACH, by
569 adjusting the assumed surface pH from 6.68 to 8 (justifiable given the considerable dust
570 emissions in the region (Zhang et al., 2018)), the model V_d moved closer to the aircraft-derived
571 values (Figure 5b), reducing the model-observation gap by approximately 2/3. In addition,
572 substituting the aerodynamic resistance and quasi-laminar sublayer resistance parameterizations
573 in the GEM-MACH algorithm with that from Zhang et al. (2002) and NOAA-GEM (Wu et al.,

574 2018), respectively, resulted in a further increase in the model V_d distribution that encompasses
575 most of the observations (Figure 5b). Clearly, different algorithms respond differently to
576 changes in the parameterizations, and validation and adjustment to each algorithm needs
577 measurement-based results over large regions such as derived here.

578

579 **4 Conclusions**

580 The atmospheric transport distances and lifetimes $d_{1/e}$ and τ determined from the aircraft
581 measurements are substantially shorter than the GEM-MACH model predictions, and the dry
582 deposition fluxes F and velocities and V_d near sources are larger compared to the predictions by
583 GEM-MACH and five inferential dry deposition velocity algorithms, respectively. There are
584 important implications for these measurement-model discrepancies. Such discrepancies indicate
585 that regional or global chemical transport models using these algorithms are biased low for local
586 deposition and high for long-range transport and deposition, and **TOS** and **TON** loss from the
587 atmosphere are significantly under-predicted, resulting in overestimated lifetimes. While the
588 measurements took place over a relatively short time period, these results indicate that TOS and
589 TON may be removed from the atmosphere at about twice the rate as predicted by current
590 atmospheric deposition algorithms. This, in turn, implies a potentially significant impact on
591 deposition over longer time scales (potentially weeks to months) and relevance towards
592 cumulative environmental exposure metrics such as critical loads and their exceedance. A faster
593 near-source deposition velocity for emitted reactive gases may imply less S and N mass being
594 available for long range transport, reducing concentrations and deposition further downwind.
595 The near-source higher deposition velocity, thus has the important implication of a reduction in
596 more distant and longer timescale deposition for locations further from the sources. Moreover,

597 emissions assessed through network measurements or budget analysis of atmospheric **TOS** and
598 **TON** (Sickles and Shadwick, 2015; Paulot et al., 2018; Berglen et al., 2004) may be
599 underestimated due to lower V_d used in these estimates, and may require reassessing the
600 effectiveness of control policies. Shorter τ for **TOS** and **TON** reduces their atmospheric spatial
601 scale and intensity of smog episodes, potentially reducing human exposures (Moran et al., 2010).
602 Importantly, shorter τ for **TOS** and **TON** reduces their contribution to atmospheric aerosols;
603 consequently, the negative direct and indirect radiative forcing from these sulfur and nitrogen
604 aerosols are reduced, reducing their cooling effects on climate (Solomon et al., 2007). These
605 impacts suggest that more measurements to determine τ and F for these pollutants across large
606 geographic scales and different surface types are necessary to better quantify their climate and
607 environmental impacts in support of policy. While in the past such determination was difficult
608 and/or impossible, the present study provides a viable methodology to achieve such a goal.

609

610

611 **Table 1.** Average observed meteorological conditions and facility emission rates of **TOS** (E_{TOS})
 612 and **TON** (E_{TON}), (determined from extrapolated (to distance=0) transfer rates; Figure 1) for
 613 **TOS** and **TON** during the F7, F19 and F20 flights. SP=south plume; NP=north plume.

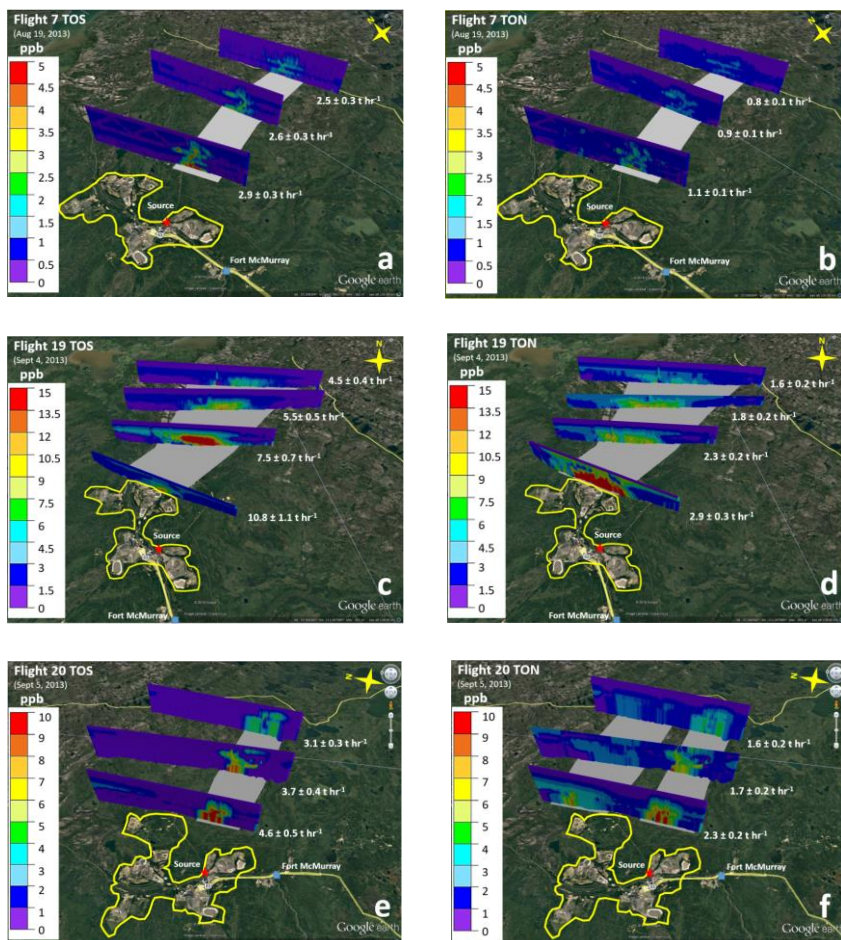
Flight	Date	Time (UTC)	Mean wind speed (m/s)	Mean wind direction (°)	Mixed layer height (m agl)	E_{TOS} (t/hr)	E_{TON} (t/hr)
7	Aug 19/13	2007–0108	13.0±1.0	256±11.7	2500±100	3.4	1.2
19	Sep 4/13	1854–2353	9.5±1.9	218±16	1200±100	18.5	3.9
20	Sep 5/13	1933–2436	8.9±1.2	281±11	2100±100	5.8	2.2 (SP) 1.2 (NP)

614

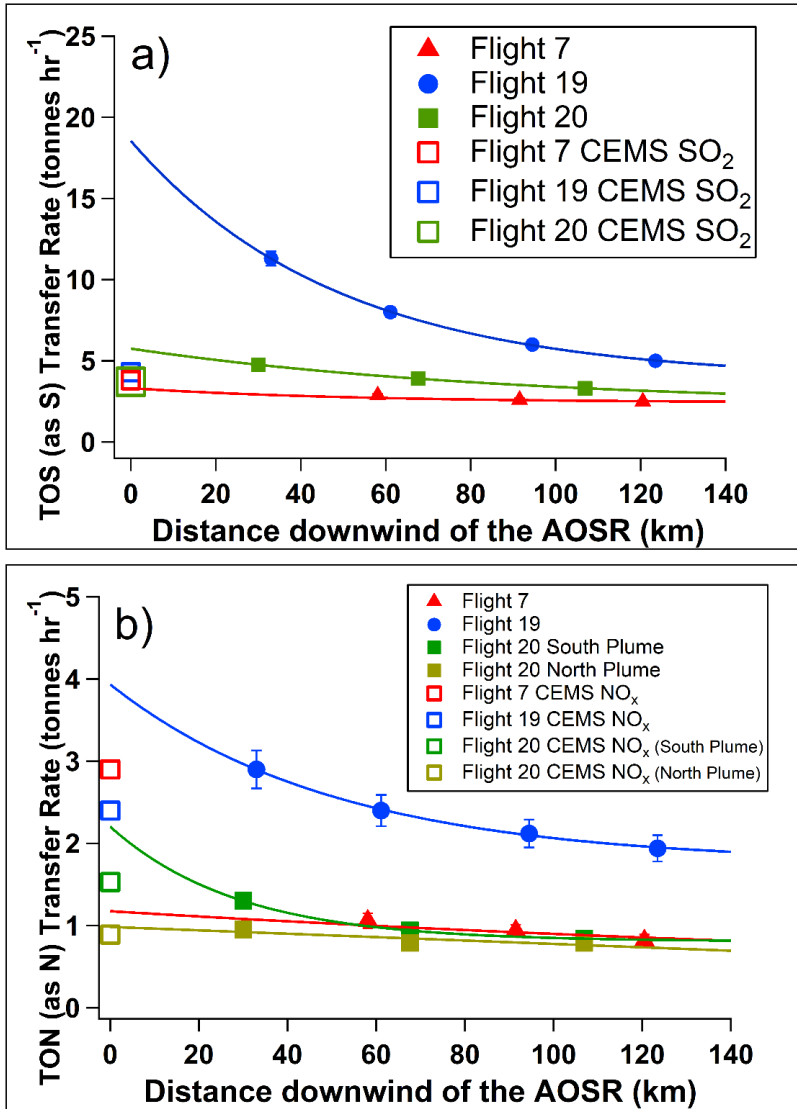
615 **Table 2.** Model average meteorological conditions and facility emission rates of **TOS** (E_{TOS}) and
 616 **TON** (E_{TON}) during the F7, F19 and F20 flights as described above. SP=south plume; NP=north
 617 plume.

Flight	Date	Time (UTC)	mean wind speed (m/s)	mean wind direction (°)	mixed layer height (m agl)	E_{TOS} (t/hr)	E_{TON} (t/hr)
7	Aug 19/13	2007–0108	12.6±0.3	253±5.0	1670±80	3.8	2.9
19	Sep 4/13	1854–2353	8.1±1.0	225±4.6	1450±43	4.3	2.4
20	Sep 5/13	1933–2436	9.1±0.7	275±1.6	1590±42	3.7	1.5 (SP) 0.9 (NP)

618

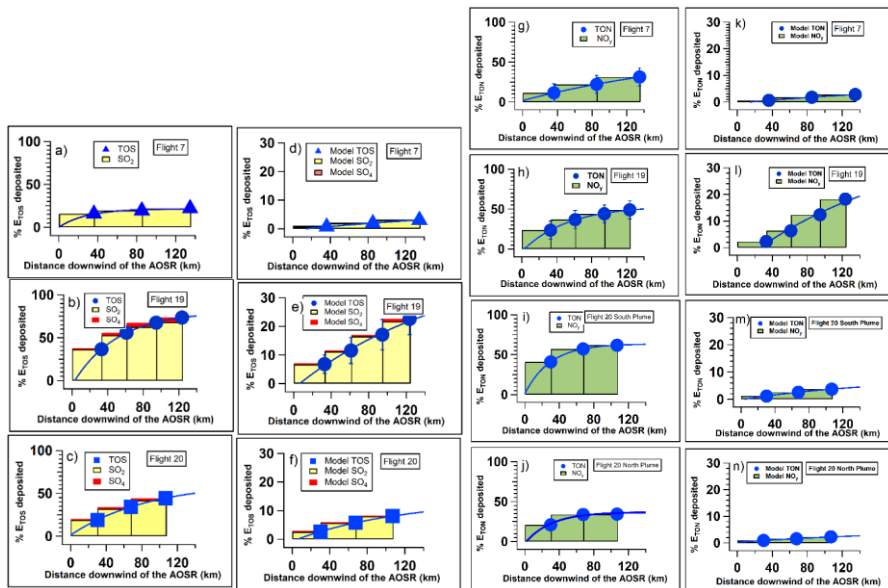


619
 620
 621 **Figure 1.** TOS (total oxidized sulfur) and TON (total oxidized nitrogen) plumes downwind of
 622 the AOSR during three Lagrangian flights, F7, F19 and F20. The AOSR facilities are enclosed
 623 by the yellow outline. The transfer rates T in t S or N hr⁻¹ across each screen are shown. The
 624 grey shaded surface areas are identified as the geographic footprint under the plumes. Data:
 625 Google Image © 2018 Image Landsat / Copernicus.

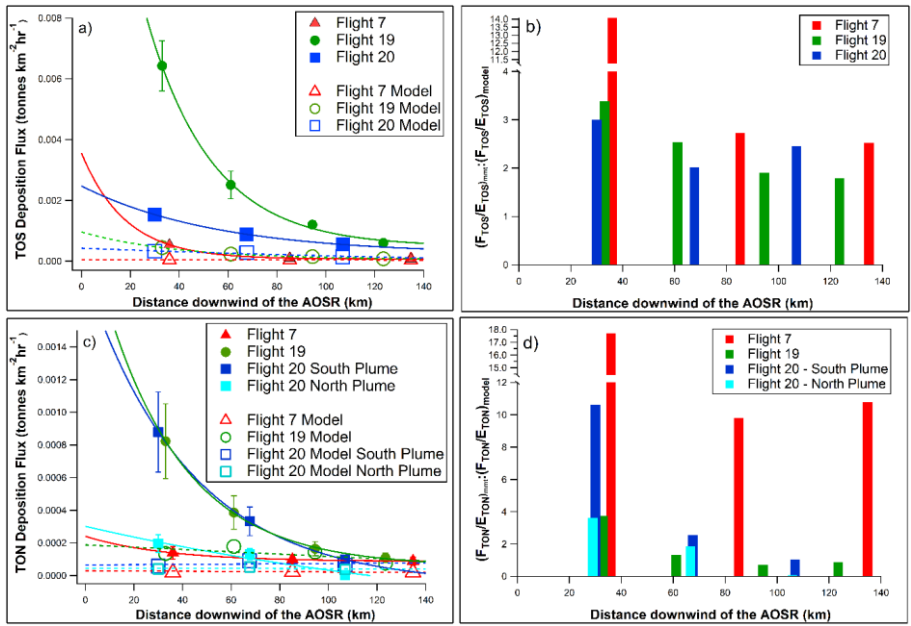


626
 627 **Figure 2.** TERRA-derived transfer rates of (a) TOS and (b) TON for F7, F19 and F20. The
 628 vertical bars indicate the propagated uncertainties. The model emission rates E_{TOS} and E_{TON} are
 629 shown by the open symbols.

630



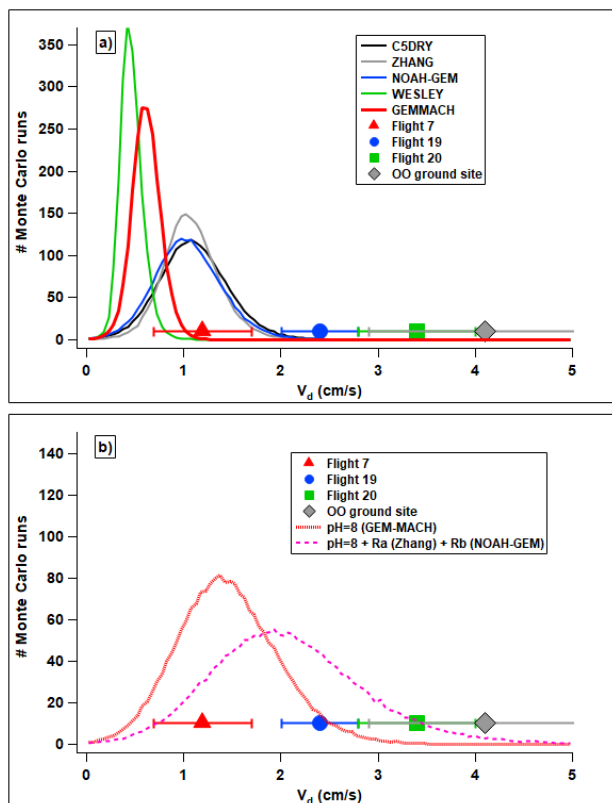
631 **Figure 3.** Cumulative dry deposition as a percentage of emissions E_{TOS} (a to f) or E_{TON} (g to n)
 632 for F7, F19 and F20 measurements with corresponding GEM-MACH model predictions. The
 633 bars show the dry deposition due to SO_2 and pSO_4 . The curves were fitted to the **TOS** and **TON**
 634 dry deposition percentages from which $d_{1/e}$ and τ were determined.



635

636 **Figure 4.** Dry deposition fluxes F_{TOS} and F_{TON} (in $t\ km^{-2}\ hr^{-1}$) determined from measurements
 637 (solid symbols) and GEM-MACH model predictions (open symbols). (a) F_{TOS} , (b) ratios of
 638 measurement to model normalized emissions F_{TOS}/E_{TOS} , (c) F_{TON} , and (d) ratios of measurement
 639 to model normalized emissions F_{TON}/E_{TON} .

640



641

642 **Figure 5.** (a) Distributions of V_d for SO_2 from Monte-Carlo simulations using 5 different
 643 deposition parameterizations (Wu et al., 2018; Makar et al., 2018) and (b) Monte-Carlo
 644 simulations for the GEM-MACH algorithm using a pH=8 and using a pH=8 plus replacing the
 645 GEM-MACH algorithm R_a and R_b formulae with that from Zhang et al. (2002) and NOAH-GEM
 646 (Wu et al., 2018), respectively. Aircraft-derived V_d for F7, F19 and F20 as well as the median
 647 value for the Oski-otin ground site (SI Figure S5) are shown in both (a) and (b) for comparison.
 648

649 **References**

- 650 Aubinet, M., Vesala, T. and Papale, D. (Eds.): Eddy Covariance. Springer Atmospheric Sciences,
651 Springer, Dordrecht, 2012.
- 652 Baldocchi, D.D., Vogel, C.A., and Hall, B.: A canopy stomatal resistance model for gaseous
653 deposition to vegetated surfaces, *Atmos. Env.*, **21**, 91-101, [https://doi.org/10.1016/0004-](https://doi.org/10.1016/0004-6981(87)90274-5)
654 [6981\(87\)90274-5](https://doi.org/10.1016/0004-6981(87)90274-5), 1987.
- 655 Baray, S., Darlington, A., Gordon, M., Hayden, K.L., Leithead, A., Li, S.-M., Liu, P.S.K.,
656 Mittermeier, R.L., Moussa, S.G., O'Brien, J., Staebler, R., Wolde, M., Worthy, D. and
657 McLaren, R.: Quantification of methane sources in the Athabasca Oil Sands Region of
658 Alberta by aircraft mass balance, *Atmos. Chem. Phys.*, **18**, 7361-7378,
659 <https://doi.org/10.5194/acp-18-7361-2018>.
- 660 Benkovitz, C.M., Schwartz, S.E., Jensen, M.P., Miller, M.A., Easter, R.C. and Bates, T.S.:
661 Modeling atmospheric sulfur over the Northern Hemisphere during the Aerosol
662 Characterization Experiment 2 experimental period, *J. Geophys. Res.*, **109**, D2220,
663 <https://doi.org/10.1029/2004JD004939>, 7, 2004.
- 664 Berglen, T.F., Berntsen, T.K., Isaksen, I.S.A. and Sundet, J.K.: A global model of the coupled
665 sulfur/oxidant chemistry in the troposphere: The sulfur cycle, *J. Geophys. Res.*, **109**, D19310,
666 <https://doi.org/10.1029/2003JD003948>, 2004.
- 667 Bobbink, R., Hicks, K., Galloway, J., Spranger, T., Alkemade, R., Ashmore, M., Bustamante,
668 M., Cinderby, S., Davidson, E., Dentener, F., Emmett, B., Erisman, J-W., Fenn, M., Gilliam,
669 F., Nordin, A., Pardo, L. and De Vries, W.: Global assessment of nitrogen deposition effects
670 on terrestrial plant diversity: a synthesis, *Ecol. Appl.* **20**, 30-59, [https://doi.org/10.1890/08-](https://doi.org/10.1890/08-1140.1)
671 [1140.1](https://doi.org/10.1890/08-1140.1), 2010.
- 672 Brook, J.R., Di-Giovanni, F., Cakmak, S. and Meyers, T.P.: Estimation of dry deposition
673 velocity using inferential models and site-specific meteorology – uncertainty due to siting of
674 meteorological towers, *Atmos. Environ.*, **31**, 3911-3919, [https://doi.org/10.1016/S1352-](https://doi.org/10.1016/S1352-2310(97)00247-1)
675 [2310\(97\)00247-1](https://doi.org/10.1016/S1352-2310(97)00247-1), 1997.
- 676 Chin, M., Savoie, D.L., Huebert, J., Bandy, A.R., Thornton, D.C., Bates, T.S., Quinn, P.K.,
677 Saltzman, E.S. and De Bruyn, W.J.: Atmospheric sulfur cycle simulated in the global model
678 GOCART: Comparison with field observations and regional budgets, *J. Geophys. Res.*, **105**,
679 24689-24712, <https://doi.org/10.1029/2000JD900384>, 2000.
- 680 Christian, G., Ammann, M., D'Anna, B., Donaldson, D.J. and Nizkorodov, S.A.: Heterogeneous
681 photochemistry in the atmosphere, *Chem. Rev.* **115**, 4218-4258,
682 <https://doi.org/10.1021/cr500648z>, 2015.
- 683 DeCarlo, P.F. , Kimmel, J.R., Trimborn, A., Northway, M.J., Jayne, J.T., Aiken, A.C., Gonin,
684 M., Fuhrer, K., Horvath, T., Docherty, K.S., Worsnop, D.R., Jimenez, J.L.: Field-
685 deployable, high-resolution, time-of-flight aerosol mass spectrometer, *Anal. Chem.*, 8281-
686 9289, <https://doi.org/10.1021/ac061249n>, 2006.

687 de Gouw, J. and Warneke, C.: Measurements of volatile organic compounds in the earth's atmosphere
688 using proton-transfer-reaction mass spectrometry, *Mass Spectrom. Rev.*, 26, 223-257,
689 <https://doi.org/10.1002/mas.20119>, 2007.

690 Degrazia, G.A., Maldaner, S., Buske, D., Rizza, U., Buligon, L., Cardoso, V., Roberti, D.R.,
691 Acevedo, O., Rolim, S.B.A. and Stefanello, M.B.: Eddy diffusivities for the convective
692 boundary layer derived from LES spectral data, *Atmos. Pollut. Res.*, 6, 605-611,
693 <https://doi.org/10.5094/APR.2015.068>, 2015.

694 Dentener, F., Drevet, J., Lamarque, J.F., Bey, I., Eickhout, B., Fiore, A.M., Hauglustaine, D.,
695 Horowitz, L.W., Krol, M., Kulshrestha, U.C., Lawrence, M., Galy-Lacaux, C., Rast, S.,
696 Shindell, D., Stevenson, D., Van Noije, T., Atherton, C., Bell, N., Bergman, D., Butler, T.,
697 Cofala, J., Collins, B., Doherty, R., Ellingsen, K., Galloway, J., Gauss, M., Montanaro, V.,
698 Müller, J.F., Pitari, G., Rodriguez, J., Sanderson, M., Solmon, F., Strahan, S., Schultz, M.,
699 Sudo, K., Szopa, S. and Wild, O.: Nitrogen and sulfur deposition on regional and global
700 scales: A multimodel evaluation, *Global Biogeochem. Cycle*, 20, GB4003,
701 <https://doi.org/10.1029/2005GB002672>, 2006.

702 Doney, S.C. The growing human footprint on coastal and open-ocean biogeochemistry, *Science*
703 328, 1512-1516, DOI: 10.1126/science.1185198, 2010.

704 Dunlea, E.J. Herndon, S.C., Nelson, D.D., Volkamer, R.M., San Martini, F., Sheehy, P.M.,
705 Zahniser, M.S. Shorter, J. H., Wormhoudt, J. C., Lamb, B. K., Allwine, E. J., Gaffney, J. S.,
706 Marley, N. A., Grutter, M., Marquez, C., Blanco, S., Cardenas, B., Retama, A., Ramos
707 Villegas, C. R., Kolb, C. E., Molina, L. T., and Molina, M. J.: Evaluation of nitrogen dioxide
708 chemiluminescence monitors in a polluted urban environment, *Atmos. Chem. Phys.*, 7,
709 2691–2704, <https://doi.org/10.5194/acp-7-2691-2007>, 2007.

710 Emerson, E.W., Hodshire, A.L., DeBolt, H.M., Bilsback, K.R., Pierce, J.R., McMeeking, G.R.,
711 and Farmer, D.K., Revisiting particle dry deposition and its role in radiative effect estimates,
712 *Proc. Natl. Acad. Sci. U.S.A.*, 117 (42), 26076-26082, doi: 10.1073/pnas.2014761117, 2020.

713 Finkelstein, P.L., Ellestad, T.G., Clarke, J.F., Meyers, T.P., Schwede, D.B., Hebert E.O. and
714 Neal, J.A.: Ozone and sulfur dioxide dry deposition to forests: Observations and model
715 evaluation, *J. Geophys. Res.*, 105, 15365-15377, <https://doi.org/10.1029/2000JD900185>,
716 2000.

717 Fowler, D., Pilegaard, K., Sutton, M.A., Ambus, P., Raivonen, M., Duyzer, J., Simpson, D.,
718 Fagerli, H., Fuzzi, S., Schjoerring, J.K., Granier, C., Neftel, A., Isaksen, I.S.A., Laj, P.,
719 Maione, M., Monks, P.S., Burkhardt, J., Daemmgen, U., Neiryneck, J., Personne, E., Wichink-
720 Kruit, R., Butterbach-Bahl, K., Flechard, C., Tuovinen, J.P., Coyle, M., Gerosa, G., Loubet,
721 B., Altimir, N., Gruenhage, L., Ammann, C., Cieslik, S. Paoletti, E., Mikkelsen, T.N., Ro-
722 Poulsen, H., Cellier, P., Cape, J.N., Horváth, L., Loreto, F., Niinemets, Ü., Palmer, P.I.,
723 Rinne, J., Misztal, P., Nemitz, E., Nilsson, D., Pryor, S., Gallagher, M.W., Vesala, T., Skiba,
724 U., Brüggemann, N. Zechmeister-Boltenstern, S., Williams, J., O'Dowd, Facchini, M.C., de
725 Leeuw, G., Flossman, A., Chaumerliac, N. and Erisman, J.W.: Atmospheric composition
726 change: ecosystems-atmosphere interactions, *Atmos. Environ.*, 43,
727 <https://doi.org/10.1016/j.atmosenv.2009.07.068>, 5193-5267, 2009.

728 Fulgham, S.R., Millet, D.B., Alwe, H.D., Goldstein, A.H., Schobesberger, S., and Farmer, D.K.,
729 Surface wetness as an unexpected control on forest exchange of volatile organic acids,
730 *Geophys. Res. Lett.*, **47**, e2020GL088745, <https://doi.org/10.1029/2020GL088745>, 2020.

731 Gordon, M., Li, S.-M., Staebler, R., Darlington, A., Hayden, K., O'Brien, J. and Wolde, M.:
732 Determining air pollutant emission rates based on mass balance using airborne measurement
733 data over the Alberta oil sands operations, *Atmos. Meas. Tech.*, **8**, 3745-3765,
734 <https://doi.org/10.5194/amt-8-3745-2015>, 2015.

735 Howarth, R.W. Review: coastal nitrogen pollution: a review of sources and trends globally and
736 regionally, *Harmful Algae*, **8**, 14-20, <https://doi.org/10.1016/j.hal.2008.08.015>, 2008.

737 Jarvis, P.G. The interpretation of the variations in leaf water potential and stomatal conductance
738 found in canopies in the field, *Phil. Trans. R. Soc. Lond., B.*, **273**, 593-610,
739 <https://doi.org/10.1098/rstb.1976.0035>, 1976.

740 Li, S.-M., Leithead, A., Moussa, S.G., Liggio, J., Moran, M.D., Wang, D., Hayden, K.,
741 Darlington, A., Gordon, M., Staebler, R., Makar, P.A., Stroud, C.A., McLaren, R., Liu,
742 P.S.K., O'Brien, J., Mittermeier, R.L., Zhang, J., Marson, G., Cober, S.G., Wolde, M. and
743 Wentzell, J.J.B.: Differences between measured and reported volatile organic compound
744 emissions from oil sands facilities in Alberta, Canada, *Proc. Natl. Acad. Sci.*, **114**, E3756-
745 E3765, <https://doi.org/10.1073/pnas.1617862114>, 2017.

746 Liggio, J., Li, S.-M., Hayden, K., Taha, Y.M., Stroud, C., Darlington, A., Drollette, B.D.,
747 Gordon, M. Lee, P., Liu, P., Leithead, A., Moussa, S.G., Wang, D., O'Brien, J., Mittermeier,
748 R.L., Brook, J.R., Lu, G., Staebler, R., Han, Yuemei, Tokarek, T.W., Osthoff, H.D., Makar,
749 P.A., Zhang, J., Plata, D.L. and Gentner, D.R.: Oil sands operations as a large source of
750 secondary organic aerosols, *Nature*, **534**, 91-94, <https://doi.org/10.1038/nature17646>, 2016.

751 Liggio, J., Li, S.-M., Staebler, R., Hayden, K., Darlington, A., Mittermeier, R.L., O'Brien, J.,
752 McLaren, R., Wolde, M. Worthy, D. and Vogel, F.: Measured Canadian oil sands CO2
753 emissions are higher than estimates made using internationally recommended methods,
754 *Nature Comm.*, **10**, 1863, <https://doi.org/10.1038/s41467-019-09714-9>, 2019.

755 Makar, P.A., Akingunola, A., Aherne, J., Cole, A.S., Aklilu, Y., Zhang, J., Wong, I., Hayden, K.,
756 Li, S.-M., Kirk, J., Scott, K., Moran, M.D., Robichaud, A., Cathcart, H., Baratzedah, P.,
757 Pabla, B., Cheung, P., Zheng, Q. and Jeffries, D.S.: Estimates of exceedances of critical loads
758 for acidifying deposition in Alberta and Saskatchewan, *Atmos. Chem. Phys.*, **18**, 9897-9927,
759 <https://doi.org/10.5194/acp-18-9897-2018>, 2018.

760 Matsuda, K., Watanabe, I., Wingpud, V. and Theramongkol, P.: Deposition velocity of O₃ and
761 SO₂ in the dry and wet season above a tropical forest in northern Thailand, *Atmos. Environ.*,
762 **40**, 7557-7564, <https://doi.org/10.1016/j.atmosenv.2006.07.003>, 2006.

763 Meyers, T.P., Hicks, B.B., Hosker Jr, R.P., Womack, J.D. and Satterfield, L.C.: Dry deposition
764 inferential measurement techniques. II. Seasonal and annual deposition rates of sulfur and
765 nitrate, *Atmos. Environ.*, **25**, 2631-2370, [https://doi.org/10.1016/0960-1686\(91\)90110-S](https://doi.org/10.1016/0960-1686(91)90110-S),
766 1991.

767 Moran, M.D., Ménard, S., Pavlovic, R., Anselmo, D., Antonopoulos, S., Makar, P.A., Gong, W.,
768 Gravel, S., Stroud, C., Zhang, J., Zheng, Q., Robichaud, A., Landry, H., Beaulieu, P.-A.,
769 Gilbert, S., Chen, J. and Kallaur, A.: Recent advances in Canada's national operational AQ
770 forecasting system. In: Steyn DG, Rao ST (Eds) Air Pollution Modelling and Its Application,
771 Springer, Dordrecht, 289,
772 https://www.researchgate.net/deref/http%3A%2F%2Fdx.doi.org%2F10.1007%2F978-94-007-5577-2_37, 2010.
773

774 Munger, J.W., Fan, S., Bakwin, P.S., Goulden, M.L., Goldstein, A.H., Colman, A.S. and Wolfsy,
775 S.C.: Regional budgets for nitrogen oxides from continental sources: Variations of rates for
776 oxidation and deposition with season and distance from source regions, *J. Geophys. Res.*, **103**,
777 8355-8368, <https://doi.org/10.1029/98JD00168>, 1998.

778 Paulot, F., Malyshev, S., Nguyen, T., Crouse, J.D., Shevliakova, E. and Horowitz, L.W.:
779 Representing sub-grid scale variations in nitrogen deposition associated with land use in a
780 global Earth system model: implications for present and future nitrogen deposition fluxes over
781 North America, *Atmos. Chem. Phys.* **18**, 17963-17978, [https://doi.org/10.5194/acp-18-17963-](https://doi.org/10.5194/acp-18-17963-2018)
782 [2018](https://doi.org/10.5194/acp-18-17963-2018), 2018.

783 Samset, B.H., Myhre, G., Herber, A., Kondo, Y., Li, S.-M., Moteki, N., Koike, M., Oshima, N.,
784 Schwarz, J.P., Balkanski, Y., Bauer, S.E., Bellouin, N., Berntsen, T.K., Bian, H., Chin, M.,
785 Diehl, T., Easter, R.C., Ghan, S.J., Iversen, T., Kirkevåg, A., Lamarque, J.-F., Lin, G., Liu,
786 X., Penner, J.E., Schulz, M., Seland, Ø., Skeie, R.B., Stier, P., Takemura, T., Tsigaridis, K.
787 and Zhang, K.: Modelled black carbon radiative forcing and atmospheric lifetime in AeroCom
788 Phase II constrained by aircraft observations, *Atmos. Chem. Phys.* **14**, 12465–12477,
789 doi:10.5194/acp-14-12465-2014, 2014.

790 Sickles, J.E. & Shadwick, D.S. Air quality and atmospheric deposition in the eastern US: 20
791 years of change. *Atmos. Chem. Phys.*, **15**, 173-197, <https://doi.org/10.5194/acp-15-173-2015>,
792 2015.
793

794 Solomon, S., Quin, M., Manning, Z., Chen, M. Marquis, K.B., Averyt, M., Tignor, M., and
795 Miller, H.L. (Eds): *Climate Change 2007: The Physical Science Basis, IPCC AR4*,
796 Cambridge University Press, 2007.

797 Stull, R. *Introduction to Boundary Layer Meteorology*, Kluwer Academic Press, 1988.

798 Vet, R., Artz, R.S., Carou, S., Shaw, M., Ro, C.-U., Aas, W., Baker, A., Bowersox, V.C.,
799 Dentener, F., Galy-Lacaux, C., Hou, A., Pienaar, J., Gillett, R., Forti, M.C., Gromov, S., Hara,
800 H., Khodzher, T., Mahowald, N.M., Nickovic, S., Rao, P.S.P. and Reid, N.W.: A global
801 assessment of precipitation chemistry and deposition of sulfur, nitrogen, sea salt, base cations,
802 organic acids, acidity and pH, and phosphorus, *Atmos. Environ.*, **93**, 3-100,
803 <https://doi.org/10.1016/j.atmosenv.2013.10.060>, 2014.

804 Wesley, M.L. Parameterization of surface resistances to gaseous dry deposition in regional-scale
805 numerical models, *Atmos. Environ.*, **23**, 1293-1304,
806 [https://ui.adsabs.harvard.edu/link_gateway/1989AtmEn..23.1293W/doi:10.1016/0004-](https://ui.adsabs.harvard.edu/link_gateway/1989AtmEn..23.1293W/doi:10.1016/0004-6981(89)90153-4)
807 [6981\(89\)90153-4](https://ui.adsabs.harvard.edu/link_gateway/1989AtmEn..23.1293W/doi:10.1016/0004-6981(89)90153-4), 1989.

- 808 Wesley, M.L. & Hicks, B.B. A review of the current status of knowledge on dry deposition,
809 Atmos. Environ., **34**, 2261-2282,
810 [https://ui.adsabs.harvard.edu/link_gateway/2000AtmEn..34.2261W/doi:10.1016/S1352-](https://ui.adsabs.harvard.edu/link_gateway/2000AtmEn..34.2261W/doi:10.1016/S1352-2310(99)00467-7)
811 [2310\(99\)00467-7](https://ui.adsabs.harvard.edu/link_gateway/2000AtmEn..34.2261W/doi:10.1016/S1352-2310(99)00467-7), 2000.
812
- 813 WHO, Ambient Air Pollution: A Global Assessment of Exposure and Burden of Disease, 2016.
814
- 815 Williams, E.J., Baumann, K., Roberts, J.M., Bertman, S.B., Norton, R.B., Fehsenfeld, F.C.,
816 Springston, S.R., Nennermacker, L.J., Newman, L., Olszyna, K., Meagher, J., Hartsell, B.,
817 Edgerton, E., Pearson, J.R., and Rodgers, M.O., Intercomparisons of ground-based NO_y
818 measurement techniques, J. Geophys. Res., 103, 22,621-22,280,
819 <https://doi.org/10.1029/98JD00074>, 1998.
820
- 821 Wright, L.P., Zhang, L., Cheng, I. and Aherne, J.: Impacts and effects indicators of atmospheric
822 deposition of major pollutants to various ecosystems - a review, Aerosol Air Quality Res., **18**,
823 1953-1992, <https://doi.org/10.4209/aaqr.2018.03.0107>, 2018.
824
- 825 Wu, Z., Schwede, D.B., Vet, R., Walker, J.T. Shaw, M. Staebler, R. and Zhang, L.: Evaluation
826 and intercomparison of five North American dry deposition algorithms at a mixed forest site,
827 J. Adv. Mod. Earth Sys., **10**, 1571-1586, <https://doi.org/10.10292017MS001231>, 2018.
- 828 Zhang, L., Moran, M.D., Makar, P., and Brook, J.R.: Modelling gaseous dry deposition in
829 AURAMS: a unified regional air-quality modelling system, Atmos. Environ., **36**, 537-560,
830 2002. Zhang, J., Moran, M.D., Zheng, Q., Makar, P.A., Baratzadeh, P., Marson, G., Liu, P.
831 and Li, S.-M.: Emissions preparation and analysis for multiscale air quality modeling over
832 the Athabasca Oil Sands Region of Alberta, Canada, Atmos. Chem. Phys., **18**, 10459-
833 10481, <https://doi.org/10.5194/acp-18-10459-2018>, 2018.

834

835 **Author Contribution:**

836 KH, SML, JL, SM, RM, RS, JO, MW all contributed to the collection of aircraft observations in the field.
837 KH, RM and JO made the SO₂, NO_y, and pSO₄ measurements and carried out subsequent QA/QC of data.
838 RM analyzed canister VOCs and provided OH concentration estimates. SM provided OH estimates from
839 MCM modelling as a comparison. AD contributed to the development of TERRA. JL wrote the Monte
840 Carlo code. PM and AA ran the model and provided model analyses. JZ provided emissions data. LZ and
841 RS provided deposition algorithm parameters. KH and SML wrote the paper input from all co-authors.

842 **Code availability**

843 All the computer code associated with the TERRA algorithm, including for the kriging of pollutant data, a
844 demonstration dataset and associated documentation is freely available upon request. The authors request
845 that future publications which make use of the TERRA algorithm cite this paper, Gordon et al., Liggio et
846 al., or Li et al. as appropriate.

847 **Data availability**

848 All data used in this publication are freely available on the Canada-Alberta Oil Sands Environmental
849 Monitoring Information Portal: [https://www.canada.ca/en/environment-climate-change/services/oil-](https://www.canada.ca/en/environment-climate-change/services/oil-sands-monitoring/monitoring-air-quality-alberta-oil-sands.html)
850 [sands-monitoring/monitoring-air-quality-alberta-oil-sands.html](https://www.canada.ca/en/environment-climate-change/services/oil-sands-monitoring/monitoring-air-quality-alberta-oil-sands.html)
851

852 **Acknowledgements:**

853 The authors thank the National Research Council of Canada flight crew of the Convair-580, the
854 Air Quality Research Division technical support staff, Julie Narayan for in-field data
855 management support, and Stewart Cober for the management of the study. The project was
856 funded by the Air Quality program of Environment and Climate Change Canada and the Oil
857 Sands Monitoring (OSM) program. It is independent of any position of the OSM program.
858

859 The authors declare no competing interests.